Angle-resolved photoemission spectroscopy study on the Fermi surface topology of $Na_x CoO_2$

H-B Yang[1], Z Wang and H Ding

Department of Physics, Boston College, Chestnut Hill, MA 02467, USA

Abstract

We report a systematic study on $Na_x CoO_2$ ($0.3 \leqslant x \leqslant 0.72$) using angle-resolved photoemission spectroscopy (ARPES), with a focus on the Fermi surface topology of the metallic samples. Within this doping range, we observed only one large hexagonal Fermi surface around the Γ-point, which comes from the a_{1g} band. Contrary to most band calculations, our results show that the e'_g bands never cross the Fermi level to form small Fermi surface pockets near the K-point. The enclosed area of the a_{1g} Fermi surface is found to be consistent with the Luttinger theorem within the doping range in this study. We also found that, at $x = 1/3$, the Fermi surface coincides with the zone boundary of the $\sqrt{3} \times \sqrt{3}$ commensurate ordering, indicating the importance of charge fluctuations in this material.

(Some figures in this article are in colour only in the electronic version)

1. Introduction

Since the discovery of the high-T_c (high critical temperature) cuprates over 20 years ago, researchers have been wondering if this unconventional superconductivity exits only in the copper oxides, or whether it can be found in other 3d transition metal oxides (TMOs). For a long time the cuprates were the only TMOs known to become superconductors. Finally, in 2003, superconductivity was discovered in an oxide compound of cobalt, a transition metal element that is close to copper in the periodic table. The material, $Na_x CoO_2 \cdot yH_2O$ ($T_c \sim 5$ K), was accidentally discovered by Takada and his co-workers when they introduced water into $Na_x CoO_2$ [1]. As water mysteriously makes this cobaltate a superconductor, it is sometimes called the 'ice-superconductor'.

However, sodium-doped cobalt oxide is not a new material. It had been studied for several years before the 2003 discovery for its potential as a good thermoelectric material. In 1997, Terasaki and co-workers discovered a large thermoelectric power in $Na_x CoO_2$

[1] Present address: Condensed Matter and Materials Science Department, Brookhaven National Laboratory, Upton, NY 11973, USA.

$(0.5 \leqslant x \leqslant 0.75)$ [2]. Their finding was quite a surprise at that time, sine it is against the common wisdom that dirty conductors are not suitable for thermoelectric materials, and most good thermoelectric materials are indeed narrow-gap semiconductors with high mobility.

Remarkably, a recent report [3] showed that when the Na content increases to over 0.75, both the thermopower (S) and the figure of merit (Z) are enhanced significantly, making the cobaltate a promising candidate for low-temperature thermoelectric applications. While it is generally believed that many-body interactions and the frustrations associated with triangular lattice, both of which induce narrow band and strong magnetic correlations, are responsible for the unusually large thermopower in this material, the exact mechanism is still largely unknown.

The discovery of superconductivity in the hydrated cobaltate is even more surprising, and it made a splash in the condensed matter physics community. There are many similarities between the cobaltate and the high-T_c cuprates, and many believe that research in the cobaltate might shed some light on the long-standing high-T_c problem. Like the cuprates, the cobaltate is a 3d-valence transition metal oxide, and the large on-site Coulomb repulsion (U) of Co 3d electrons, estimated to be $\sim$3–5 eV by satellite features for both core levels and valence band [4, 5], should make it a highly correlated electron system since the bandwidth is small. In addition, the cobaltate also has a layered structure, in which the CoO_2 layer is the conducting layer, just like the CuO layer in the cuprates. Adding water molecules between the CoO_2 layers increases the c-axis significantly, thus making the system more two-dimensional (2D), indicating the importance of the two-dimensionality just like in the cuprates. The two-dimensionality of the cobaltate has also made it a suitable material for angle-resolved photoemission spectroscopy (ARPES) experiments. These similarities have attracted many researchers working in the field of high-T_c superconductivity to conduct comparison studies of this new superconductor.

However, it is important to realize that there are some significant differences between the cobaltate and the cuprates. First of all, unlike the cuprates, which form a 2D square lattice in the Cu–O plane, the cobaltate forms a triangular (or hexagonal) lattice. It is well known that while it is easy to stabilize the antiferromagnetic (AFM) ordering in the square lattice, the triangular lattice frustrates the AFM spin configuration. This frustration may lead to the realization of a spin-liquid or RVB state in this material [6, 7]. Second, the top valence electrons in the cobaltate are from the t_{2g} orbitals, not from the e_g orbitals as in the case of cuprates. All the three t_{2g} bands are predicted by band calculations to be close to the Fermi energy (E_F), making it a possible candidate for a multi-orbital correlated system, at least the inter-orbital correlations are much more important in this material compared to the cuprates. Third, the magnetic exchange energy J is very small ($\sim$a few millielectronvolts [8, 9]) for the cobaltate, in sharp contrast to the much larger J value ($\sim$120 meV) in the cuprates. All of these make the physics of the cobaltate interesting and unique.

The phase diagram of the cobaltate $Na_xCoO_2 \cdot yH_2O$, with varying Na content x and water intercalation y over a wide range, is very rich and complicated. As first reported by Foo *et al* [10], the ground state of Na_xCoO_2 can be regarded as paramagnetic metal when at $x < 0.5$, and it evolves into a 'Curie–Weiss metal' as x increases to above 0.5, and eventually reaches spin-density-wave (SDW) state at $x > 0.75$. In between, there is a peculiar insulating state at $x = 0.5$, which exhibits Na ordering (below $\sim$410 K) [11, 12], magnetic ordering (below $\sim$88 K) [13, 14], and change ordering which finally triggers the metal–insulator transition (below $\sim$53 K) [10], with a small energy gap ($2\Delta \sim 15$ meV) observed first by optical experiments [15, 16]. With proper water intercalation ($y = 1.3$ and two layers of water molecules per unit cell), the cobaltate becomes superconducting in the vicinity of $x = 1/3$, possibly forming a dome-shape region in the T–x phase diagram [17], somewhat similar to the case of cuprates. However, the exact position and shape of superconducting phase are currently controversial. There are few experimental results for $x < 0.3$ and $x > 0.85$ due to lack of

good-quality samples in these regions. It is believed that when x approaches 0, the system becomes a Mott insulator because Co^{4+} leaves a single hole in the t_{2g} orbitals, although the scenario of a multi-orbital Fermi surface would invalidate this half-filling condition. At the other extreme of doping (x approaches 1), it is almost certain that the system becomes a band insulator. Whether Na_xCoO_2 should be considered as an electron-doped Mott insulator or a hole-doped band insulator remains unsettled, although the results from optical conductivity support the latter claim [18].

Understanding the electronic structure and the Fermi surface (FS) topology is the first step toward understanding the diverse physical properties and the nature of the pairing interaction in the cobaltate. Theoretically, a first-principles band calculation on $Na_{0.5}CoO_2$ was first carried out by Singh in 2000 using the local density approximation (LDA) [19]. In the calculation, the t_{2g} manifold in $Na_{0.5}CoO_2$ is further split by the rhombohedral crystal field into one a_{1g} and two e'_g bands. Two kinds of Fermi surface are predicted as well. (1) A large cylindrical hole-like Fermi surface around the Γ–A line, which has dominant a_{1g} character; (2) small hole-like Fermi surface pockets centered around 2/3 of the way out on the Γ–K direction, which have mostly e'_g characters. These predictions were confirmed by subsequent LDA calculations [20, 21]. In particular, a recent LDA calculation predicted that the large density of states (DOS) contributed from the six FS pockets and the nesting condition among them enhance the spin fluctuations which lead to superconducting pairing of the quasiparticles (QPs) on these Fermi surfaces [21].

2. Experiments

In this study, we have measured many Na_xCoO_2 single crystals with $0.3 \leqslant x \leqslant 0.72$. ARPES data on the insulating phase at $x = 0.5$ are not reproducible due to the fact that the cleave process leaves only 50% Na atoms on the surface statistically, and no long-range Na ordering can be formed on the topmost surface. A recent ARPES report on this doping level used a small-size synchrotron beam to focus on the local charge ordering patches [22]. Therefore here we only present the data on the metallic phase. High-quality Na_xCoO_2 single crystals were prepared by both flux and floating-zone methods. ARPES experiments were performed at the Synchrotron Radiation Center (University of Wisconsin, Madison, WI) and Advanced Light Source (Lawrence Berkeley National Laboratory, Berkeley, CA). During the experiments, several undulator beamlines (NIM and PGM) with different photon energies (16–110 eV) were used. All the samples were cleaved *in situ* and measured at low temperature $T = 20$–40 K (a few were measured at higher temperature, as mentioned in the text) in a vacuum better than 1×10^{-10}. Scienta electron analyzers were used with the energy resolution of 15–25 meV and momentum resolution of $\sim 0.02\,\text{Å}^{-1}$. We have taken great care to deal with surface states which occasionally appeared on some cleaved surfaces. All of results shown here are believed to be bulk representative, and have been confirmed in many single crystals synthesized differently by different sample growth groups.

3. Results

3.1. Valence bands and photon energy dependence

Although our main interest in this study is on the Fermi surface, we want to take a brief look at the valence bands first as it is often needed to have an overview before going into the details. In ARPES, a sign for a good sample surface is a clearly visible valence band dispersion. We have measured the valence bands using many different photon energies, ranging from 16 to 110 eV. We find that the band dispersion is clearly visible, as shown in figure 1(a). Here we can see two
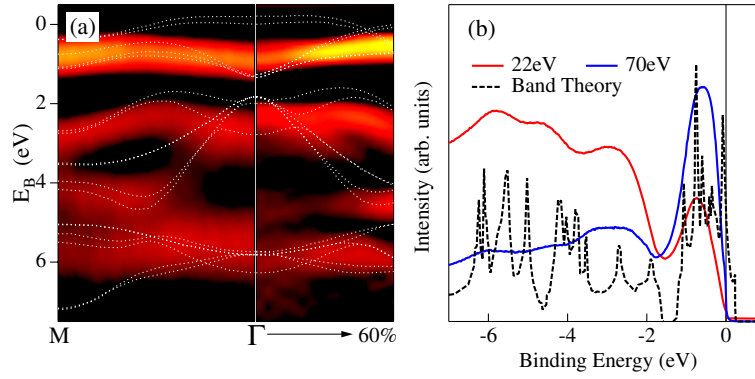
Figure 1. (a) Valence band dispersion of $Na_{0.6}CoO_2$ along Γ–M and Γ–K: comparison between second derivatives of ARPES intensity (false color plot) and LDA calculation (dashed lines) [19]. (b) Integrated spectra over a large *k*-space for 22 (red) and 70 eV (blue) photons. The dashed line is the total DOS from band theory [19]. Zero binding energy corresponds to the Fermi energy.

sets of valence bands. Right below the Fermi energy, there are the Co 3d t_{2g} bands, on which we will focus later. The other set is the O 2p bands, which locate between 2 and 8 eV in binding energy. This can be seen more clearly in figure 1(b), where we integrate the spectra over a large *k*-space to mimic the density of states at two different photon energies (22 and 70 eV). Four peaks can be identified at binding energies of 5.9, 4.6, 2.8, 0.7 eV, respectively, matching well with the band calculation shown in figure 1(b) [19]. The band calculation shows that the O 2p bands (2–7 eV) and the Co 3d bands (below 2 eV) are well separated due to a weak Co d–O p hybridization. This is clearly reflected in figure 1(b). In addition, a large enhancement of intensity for the 0.7 eV peak with 70 eV photons supports the Co 3d characters for this peak, since 70 eV is just above the Co 3p–3d resonant excitation ($\sim$63 eV).

Zooming in on the Co 3d orbitals, one can identify more dispersive features. Figure 2 displays the second derivative intensity (SDI) plots of $Na_{0.35}CoO_2$ on a smaller energy scale ($\sim$1.5 eV) along the Γ–M and Γ–K directions. By comparing to the LDA band structure for the same Na content [20], one can assign orbital characters to the dispersive features. However, the measured occupied bandwidths ($\sim$0.7–0.8 eV) are, remarkably, narrower than the calculated ones (1.3–1.4 eV), resulting in approximately a factor of two in the overall bandwidth reduction, indicating the importance of strong electron correlations in this material. Note that the flat features at the unoccupied wavevectors (*k*) visible in figures 2(a) and (b) near E_F may be due to the incoherent background often observed in correlated materials.

In ARPES, the intensity of a spectrum can be written as

$$I(\vec{k}, \omega) = I_0(\vec{k}, \nu, \vec{A}) f(\omega) A(\vec{k}, \omega), \tag{1}$$

where $\vec{k} = \vec{k}_{parallel}$ is the in-plane electron momentum, and ω is the electron binding energy with respect to the Fermi energy [23]. As photoemission only measures the occupied states, the overall intensity is multiplied by the Fermi function $f(\omega) = (e^{\omega/k_BT} + 1)^{-1}$. $A(\vec{k}, \omega)$ is the one-particle spectral function. $I_0(\vec{k}, \nu, \vec{A})$ is proportional to the squared matrix element, which depends on the electron momentum, and on the energy and polarization of the incident photon. Figure 3 shows a comparison of the spectra taken by photons of different energies. Compared to 22 eV photons, 100 eV photons enhance the intensity for Co 3d bands, for the reason mentioned above. Moreover, we can observe a much stronger QP-like peak for the a_{1g} band with 100 eV photons, as shown in figure 3(c). Therefore we chose to use 100 eV photons
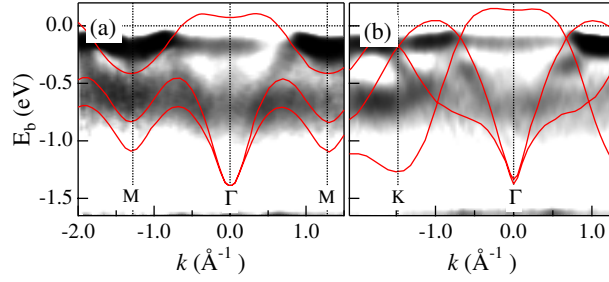
Figure 2. Co t_{2g} complex measured by ARPES (second derivative intensity plot) and calculated by LDA (red lines) [19] in $Na_{0.35}CoO_2$ along (a) Γ–M and (b) Γ–K.
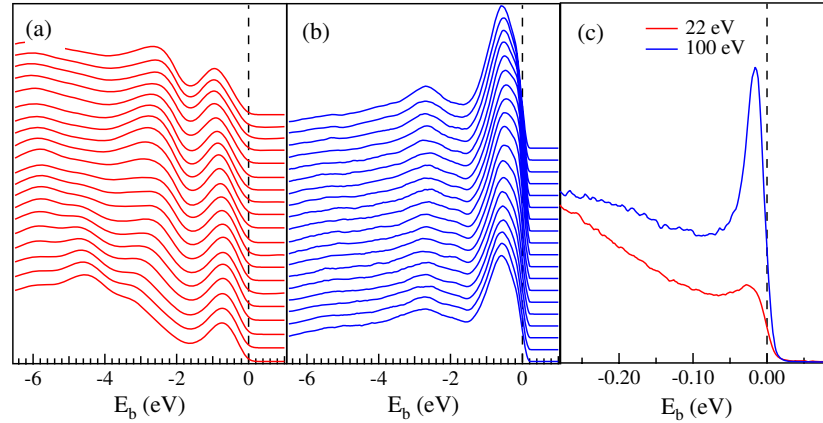

Figure 3. Energy distribution curves (EDCs) along the Γ–M direction by (a) 22 eV and (b) 100 eV photons. (c) Comparison of QP peak intensity between data from 22 and 100 eV photons.

to map the a_{1g} Fermi surface [24]. However, we found that the e'_g bands are more sensitive to 22 eV photons, as will be discussed below.

At the same time, the matrix element also depends on the emission angle of photoelectrons in such a way that a band is more visible in one particular Brillouin zone (BZ) than its neighboring zones. As an example, figure 4 shows ARPES spectra of $Na_{0.72}CoO_2$ across a wide angular range using 100 and 30 eV photons. One can see that the intensity of the a_{1g} band is stronger in the first BZ with 100 eV photons, but it is stronger in the second BZ with 30 eV photons. In our systematic ARPES studies on Na_xCoO_2, we have used various methods mentioned above to enhance certain spectral features interesting to us.

3.2. Fermi surface and low-energy excitations

To study the low-energy excitations and the FS more closely, we further zoom in near E_F (within 0.2 eV), as shown in figure 5, where a sample of $Na_{0.48}CoO_2$ is measured. During the ARPES measurement, we took many parallel cuts (five of them are shown in figures 5(b)–(f)) in k-space. It is important to have such long cuts that cover several BZs in order to accurately determine the FS, since they can help eliminate many potential problems such as sample misalignment and matrix element effects. Indeed, we have a small misalignment of about 3° in this sample, as can be seen in figure 5(g). Note that the intensity is much weaker in
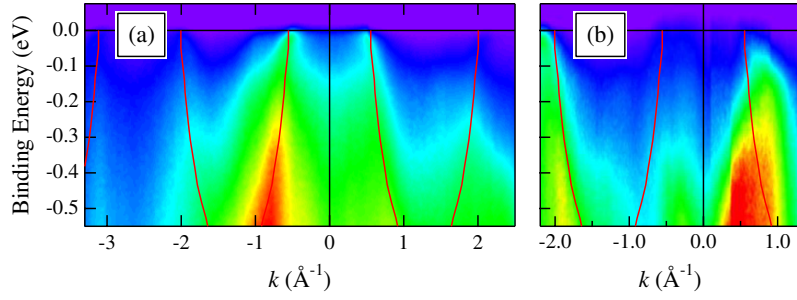
Figure 4. ARPES spectra along the Γ–M direction from (a) 100 eV and (b) 30 eV photons. Red curves show the dispersion of the a_{1g} band calculated by LDA. The spectrum covers more than two BZs in panel (a), and about one and a half BZs in panel (b).
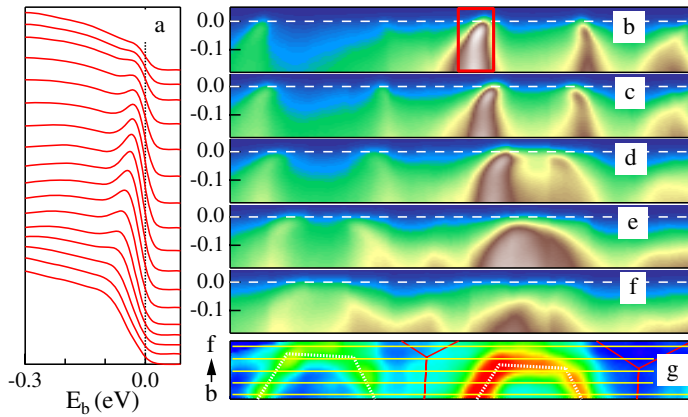
Figure 5. An example of FS mapping on $Na_{0.48}CoO_2$. (a) Representative EDCs within the red box in panel (b). (b)–(f) E–k intensity plots along the long cuts indicated by the yellow solid lines in panel (g), where FS contours obtained from the intensity at E_F, and BZ boundaries (thin red hexagons), are plotted. White dashed lines are the guides for the FSs.

the second BZ due to the photoemission matrix element effect. The FS is determined by plotting the ARPES intensity within a narrow energy window (± 2 meV) at E_F in the 2D k-space as shown in figure 5(g), where partial FS contours over two BZs are extracted from the five long cuts shown above. We also note that the low-energy band is further renormalized due to a strong 'kink' in the dispersion observed at the energy scale of 70–100 meV (see figures 5(b)–(d)).

The FS we observed, as shown in figure 5(g), corresponds to the large a_{1g} FS centered at the Γ-point predicted by the LDA calculation [19]. However, the six small FS pockets associated with the e'_g band predicted by the LDA are not present in our measurements for the entire range of $0.3 \leqslant x \leqslant 0.72$. Instead, we observed a broad peak that approaches but never reaches E_F near the K-points, as indicated by the black triangles in figure 6(a). In addition, we observed two more dispersive features. The one indicated by the green triangles belongs to the a_{1g} band, and the other indicated by the blue triangles is assigned to the other e'_g band. The reason that the intensity of the a_{1g} band is much weaker in figure 6 than in figure 5 is that different photon energies were used in the two measurements. While we used 100 eV photons in figure 5 to enhance the Co-3d character, we found that the e'_g band near the K-points is greatly enhanced at lower photon energies (30 eV in figure 6). This may suggest a stronger mixing of O 2p
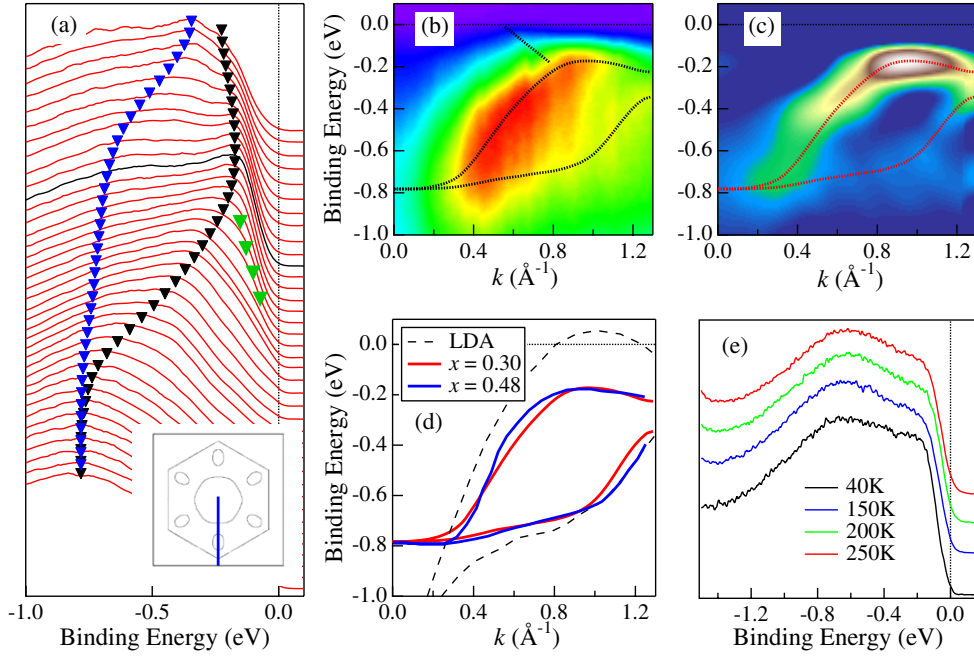
Figure 6. 'Sinking' pockets near the K-points. (a) EDCs of $Na_{0.3}CoO_2$ along Γ–K measured using 30 eV photons. Triangular markers are the guides for the band dispersion. The inset shows the location of the cut in the BZ. (b) Raw data intensity plot and (c) SDI plot for the same measurement. Red dashed lines, representing the triangular markers in panel (a), are the guides for the dispersion. (d) A comparison of the measured e'_g bands at $x = 0.3$ (red solid lines) and 0.48 (blue solid lines) to the LDA calculation [20] (black dashed lines). (e) Temperature dependence of EDC at the top of the sinking pockets.

character in the e'_g bands since the O p orbitals are more sensitive to the low-energy photons, a property often observed in the ARPES studies of cuprates.

The broad e'_g bands can be observed more clearly in the SDI plot, as shown in figure 6(b). In comparison, the measured dispersions are reminiscent of the e'_g bands calculated by the LDA [19, 20], as shown in figure 6(c). However, important differences exist: (1) the measured bandwidth is narrower than the calculated one; (2) the upper branch of the e'_g bands does not cross the Fermi level—the predicted FS pockets 'sink' below E_F. This could be associated with the opening of an energy gap at the FS. However, we did not observe clear leading-edge shift for temperatures up to 250 K, as shown in figure 6(e).

We summarize our ARPES results on the FS evolution in Na_xCoO_2 in figure 7. Figures 7(a)–(c) show three examples of the measured FS for $x = 0.3$, 0.48, and 0.72. Clearly, a single hexagonal hole-like FS, centered at the Γ-point, shrinks its size as x increases. A direct comparison of the FS contours at the four doping levels, shown in figure 7(d), provides more quantitative information on the FS evolution. All Fermi surfaces have a good hexagonal shape with parallel FS edges that can be connected by a nesting vector ($\vec{Q}_n$). The magnitude of $\vec{Q}_n$ is estimated to be $\sim$1.41, 1.40, 1.20, 1.18 Å^{-1} ($\pm$0.1 Å^{-1}) for $x = 0.3$, 0.48, 0.6, 0.72. Interestingly, these values are close to the reciprocal lattice vectors ΓK (1.47 Å^{-1}) and ΓM (1.28 Å^{-1}). In particular, the FS at $x = 0.3$ where the hydrated sample becomes superconducting, is observed to almost coincide with the reconstructed BZ of $\sqrt{3} \times \sqrt{3}$
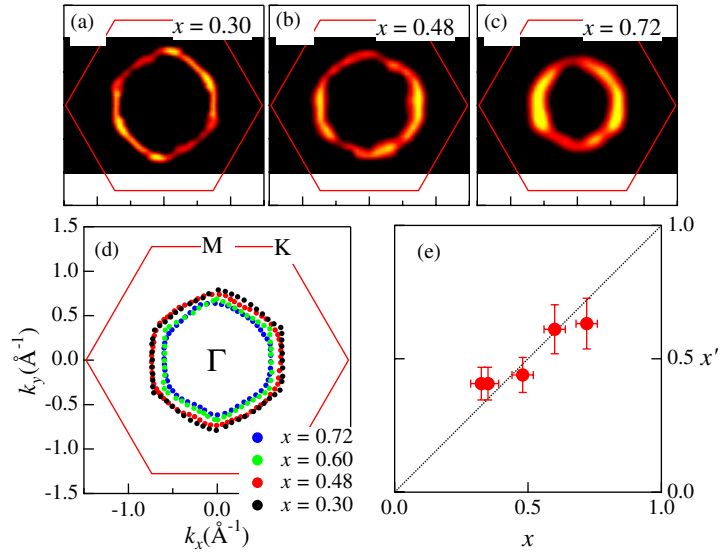
Figure 7. FS evolution in Na_xCoO_2. (a)–(c) FSs (the intensity contours at E_F) for $x = 0.3$, 0.48, and 0.72 in the first BZ (red solid lines). (d) Overlap of the FS locations at four doping levels in the BZ. (e) Effective electron doping x' derived from FS area versus Na content x. The diagonal line is from the Luttinger theorem.
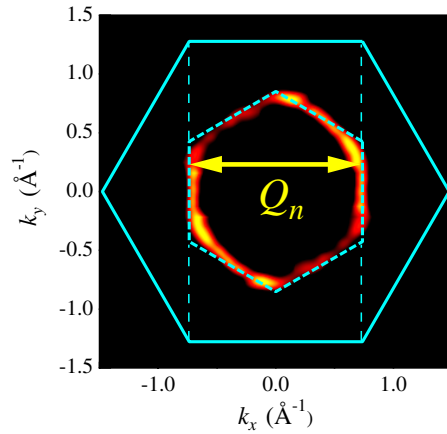
Figure 8. Overlap between the observed FS (near-E_F intensity plot) and the reconstructed BZ of $\sqrt{3} \times \sqrt{3}$ ordering in $Na_{0.3}CoO_2$.

ordering, as shown in figure 8, suggesting possible strong spin or charge fluctuations at this Na concentration. Interestingly, a recent t–V model predicted a short-range $\sqrt{3} \times \sqrt{3}$ charge ordering at both 1/3 and 2/3 filling numbers due to Coulomb jamming, but the overlap between the a_{1g} FS and this new BZ at $x = 1/3$ should enhance the charge fluctuations and even the superconducting instability at this doping level [25].

From figure 7(d), we derive the carrier density from the FS area which we call the 'effective electron doping' $x' = 1 - 2A_{FS}/A_{BZ}$, where A_{FS} is the area enclosed by the 2D FS, and A_{BZ} is the area of the BZ. In figure 7(e), x' is plotted versus the nominal Na content x. If the Luttinger

theorem is satisfied, one has $x' = x$, which is indicated by the solid line in figure 7(e). Within the experimental uncertainties, figure 7(e) shows that x' tracks well the $x' = x$ line and the Luttinger theorem is thus satisfied. The conservation of the doped electron density is quite remarkable and is consistent with the non-existence of the small FS pockets. In contrast, the FS pockets near the K-points in the LDA calculations contribute to a significant portion of the total FS area at low doping. This helps clarify the puzzle of the FS being too large in previous ARPES results [26, 27]. We note that there may exist a small jump in the FS area across $x = 0.5$, as shown in figures 7(d) and (e). It is known that the metallic states of Na_xCoO_2 are different across $x = 0.5$, with Pauli-like susceptibility for $x < 0.5$ and Curie–Weiss like for $x > 0.5$. Whether the jump is real or how it relates to the magnetic 'transition' is still an open question that needs further investigation.

4. Discussions

The observation of the 'sinking' pockets near the K-points for such a wide range of Na concentrations is very intriguing. The qualitative discrepancy with the LDA band structure points to the importance of electronic correlation effects and is a basic unresolved issue in understanding the physical properties of the cobaltate. A recent theoretical work based on the local spin density approximation (LSDA) takes into account the local Coulomb repulsion (U) using the LSDA + U approach, and finds the absence of the small FS pockets [28]. However, the disappearance of the small FS pockets in the LSDA calculation is due to the formation of a half-metal with spin-split bands and spin-polarized FSs, resulting in an FS area twice as large, which is inconsistent with our observations. It is worth pointing out that at large Na content ($x > 0.75$) the ground state of the cobaltate becomes an in-plane ferromagnetic SDW; one would expect a spin-polarized FS at low temperatures. There is a recent ARPES report that the a_{1g} Fermi surface area of $x \sim 0.8$ becomes much larger than the simple Luttinger area [29]. We have also obtained similar results, although the simple polarized FS scenario may not be sufficient for our observation. More systematic ARPES studies on high Na content samples are needed.

The absence of the e'_g FS pockets has motivated people to reexamine the LDA calculations. Surprisingly, a recent calculation from dynamic mean-field theory, which usually handles correlations better, has shown even larger FS pockets when the correlations are mild [30]. However, our calculation based on the Gutzwiller approximation has predicted the vanishing of FS pockets at all carrier concentrations under the condition of strong correlations [31]. We note that a recent LDA study has shown that the six small FS pockets can be smeared by introducing Na disorder in the calculation [32]. Thus upon water intercalation, which likely screens out the Na disorder effect, the 'sink' FS pockets may emerge above the Fermi level. However, a recent photoemission result on the hydrated cobaltate found that the top of e'_g bands is still below the Fermi energy ($\sim$20–50 meV below E_F), despite some upward shift of the leading edge [33]. In principle, the fate of small Fermi surfaces in this kind of multi-orbital system depends on a delicate balance of electron correlations, Hunds coupling, and crystal-field splitting; so does the superconductivity.

5. Conclusions

Our ARPES results on Na_xCoO_2 over a wide range of Na concentrations ($0.3 \leqslant x \leqslant 0.72$) clearly show that there is only a single hexagonal FS centered around the Γ-point. We find that the evolution of this hole-like FS obeys the Luttinger theorem. The small FS pockets near the K-points predicted by the LDA calculations are found to 'sink' below E_F with a distance to the

Fermi sea almost independent of temperature. In addition, at $x \sim 1/3$, it is observed that the hexagonal FS almost coincides with the new zone boundary of a commensurate $\sqrt{3} \times \sqrt{3}$ charge ordering, indicating the importance of charge fluctuations to the superconductivity in this material. These findings provide clear and detailed knowledge of the evolution of the electronic structure in Na_xCoO_2 and put constraints on the theoretical description of the superconductivity in the hydrated cobaltates.

Acknowledgments

References

[1] Takada K *et al* 2003 *Nature* **422** 53
[2] Terasaki I *et al* 1997 *Phys. Rev.* B **56** R12686
[3] Lee M *et al* 2006 *Preprint* cond-mat/0606426
[4] Chainani A *et al* 2004 *Phys. Rev.* B **69** 180508(R)
[5] Hasan M Z *et al* 2004 *Phys. Rev. Lett.* **92** 246402
[6] Anderson P W 1973 *Mater. Res. Bull.* **8** 153
[7] Fazekas P and Anderson P W 1974 *Phil. Mag.* **30** 23
[8] Baskaran G 2003 *Phys. Rev. Lett.* **91** 097003
[9] Bayrakci S P *et al* 2005 *Phys. Rev. Lett.* **94** 157205
[10] Foo M L *et al* 2004 *Phys. Rev. Lett.* **92** 247001
[11] Zandbergen H W *et al* 2004 *Phys. Rev.* B **70** 024101
[12] Yang H X *et al* 2005 *Solid State Commun.* **134** 403
[13] Mendels P *et al* 2005 *Phys. Rev. Lett.* **94** 136403
[14] Yokoi M *et al* 2005 *J. Phys. Soc. Japan* **74** 3046
[15] Wang N L *et al* 2004 *Phys. Rev. Lett.* **93** 147403
[16] Hwang J *et al* 2005 *Phys. Rev.* B **72** 024549
[17] Schaak R E *et al* 2003 *Nature* **424** 527
[18] Wu D, Luo J L and Wang N L 2006 *Phys. Rev.* B **73** 014523
[19] Singh D J 2000 *Phys. Rev.* B **61** 13397
[20] Lee K-W, Kine J and Pickett W E 2004 *Phys. Rev.* B **70** 045104
[21] Johannes M D *et al* 2005 *Phys. Rev.* B **71** 205103
[22] Qian D *et al* 2006 *Phys. Rev. Lett.* **96** 046407
[23] Hufner S 1996 *Photoelectron Spectroscopy: Principles and Applications* (Berlin: Springer)
[24] Yang H-B *et al* 2005 *Phys. Rev. Lett.* **95** 146401
[25] Motrunich O I and Lee P A 2004 *Phys. Rev.* B **70** 024524
[26] Yang H-B *et al* 2004 *Phys. Rev. Lett.* **92** 246403
[27] Hasan M Z *et al* 2004 *Phys. Rev. Lett.* **92** 246402
[28] Zhang P *et al* 2004 *Phys. Rev. Lett.* **93** 236402
[29] Qian D *et al* 2006 *Phys. Rev. Lett.* **96** 216405
[30] Ishida H, Johannes M D and Liebsch A 2005 *Phys. Rev. Lett.* **94** 196401
[31] Zhou S *et al* 2005 *Phys. Rev. Lett.* **94** 206401
[32] Singh D J and Kasinathan D 2006 *Preprint* cond-mat/0604002
[33] Shimojima T *et al* 2006 *Preprint* cond-mat/0606424